



INAOE

Optical spectrum analysis due to the non-collinear two-phonon light scattering by acoustic waves of finite amplitude

Technical Report No. 622

Principal contributors:

Alexandre S. Shcherbakov and Adán Omar Arellanes.

National Institute for Astrophysics, Optics, and Electronics
(INAOE), Puebla, Mexico.

National Institute for Astrophysics, Optics, and
Electronics (INAOE),

Puebla, Mexico.

Department for Optics, INAOE

INAOE, 2015

The authors hereby grant to INAOE
permission to reproduce and distribute
copies of this technical report.



Index

1. Introduction	3
2. Non-collinear two-phonon AOLS governed by acoustic waves of finite amplitude	6
3. Frequency and length of an α-Hg₂Cl₂ AOC based on the non-collinear two-phonon AOLS	10
4. Efficiency of the non-collinear two-phonon AOLS in α-Hg₂Cl₂ uniaxial crystal	14
4.1. The case of the slow shear elastic mode with $\vec{K} \parallel [110]$, $\vec{u} \parallel [1\bar{1}0]$	14
4.2. The case of the longitudinal elastic mode with $\vec{K} \parallel \vec{u} \parallel [100]$	15
5. Theoretical estimations of a dispersive component based on the calomel-made crystalline AOC	16
5.1. Realizing the Bragg regime of a two-phonon AOLS	16
5.2. Effect of the acoustic beam divergence	16
5.3. General estimations for the calomel-made AOC	16
6. Proof-of-principal experimental data	18
6.1. Experiment arrangement	18
6.2. Experimental results	20
7. Conclusion	23
8. Acknowledgments	24
9. References	24

ABSTRACT

Principally new features of square-law nonlinearity peculiar to the non-collinear two-phonon acousto-optical light scattering governed by elastic waves of finite amplitude in birefringent crystals are revealed and studied. An additional degree of freedom represented by the dispersive birefringence factor, which can be distinguished within this nonlinear phenomenon, is found and characterized. This physical degree of freedom gives us a one-of-a-kind opportunity to apply the two-phonon acousto-optical light scattering in practice for the first time. The needed theoretical analysis is developed and proof-of-principle experiments, performed with a specially designed unique wide-aperture acousto-optical cell made of the calomel (α -Hg₂Cl₂) single crystal, are presented. The results of experiments with this acousto-optical cell confirm the elaborated theory with numerical estimations and allow the proposed application to optical spectrum analysis with the doubled resolution.

Keywords: Nonlinear optics, parametric processes; Nonlinear wave mixing, Acousto-optical devices, Spectroscopy of high resolution.

1. INTRODUCTION

Application of the non-collinear acousto-optical light scattering (AOLS) to optical spectrum analysis had given rise to the non-collinear acousto-optical filters (AOFs) that have been in constant improvement since their appearance in late 1960s. Unlike the collinear AOFs, which are very restricted to a spectrum of available crystalline materials where the collinear AOLS exists, the non-collinear AOFs can work within several optically anisotropic materials. From the beginning, the most desirable material for designing the non-collinear AOFs was tellurium dioxide (TeO₂). This crystal is characterized by extremely low acoustic velocity associated with the slow shear elastic mode passing along the [110] -axis. This fact, together with moderate refractive indices and photo-elastic constant, produces a very high acousto-optical figure of merit M_2 [1]. In spite of rather large acoustic losses, which usually accompany slow elastic modes in crystals, exploiting the TeO₂-crystals makes it possible to achieve up to 100% operating efficiency at quite reasonable acoustic power densities. The spectral resolution of about 20 Å at an optical wavelength of $\lambda = 633$ nm had been achieved with an efficiency of 96% and an interaction length of ~ 50 mm [2]. Together with this, the spectral resolution of ~ 4 Å at the same wavelength had been predicted for that crystal with the optimized design [2]. Nowadays, even commercial TeO₂-based AOFs can achieve a spectral resolution 3.2 Å at $\lambda = 633$ nm with an efficiency higher than 50% [3]. Recently, studies for imaging purposes have exploited the tellurium dioxide for theoretical analysis in order to compensate the optical dispersion in a non-collinear filter to obtain better performances using the optical activity inherent in the TeO₂ crystal [4].

In recent years, the potassium dihydrophosphate (KDP) crystal had been investigated as a more profitable material for the non-collinear AOFs. This material is suitable for ultraviolet wavelengths thanks to its wide transmission range. Due to the photo-elastic tensor properties of KDP, similar AOFs have to use the slow shear elastic mode passing along a direction tilted by a few degrees to the [100]-axis, which is associated with a higher effective photo-elastic constant increasing the figure of merit. The KDP crystal is one of the most progressive materials for non-collinear AOFs in the middle to near-ultraviolet range. The KDP-based non-collinear AOFs promise significantly better performances than the existing α -quartz-based collinear AOFs that are the most widely used

and the most appropriate AOFs for the ultraviolet [5]. In particular, the KDP-crystal has a figure of merit M_2 four times higher than α -quartz crystal [6]. Past year, it has been reported that the KDP-based non-collinear AOF has been improved by enhancing the angular aperture of this AOF and achieving a spectral resolution of 2.5 \AA at $\lambda = 205 \text{ nm}$ [7].

Together with this, the mercurous chloride or calomel (α - Hg_2Cl_2) crystal is another promising material for acousto-optical devices. This material has tetragonal symmetry, anomalously small acoustic velocity for the slow shear elastic mode passing along the [110]-axis (being almost 2 times lower than in tellurium dioxide), large refractive indices and birefringence, and promises a really high figure of merit M_2 . Initially, the acousto-optic properties of small-size samples of this material had been studied in 1976, and later crystals of about 50 mm long were investigated [8]. The longitudinal acoustic mode (in several directions) can be exploited as well, but the figure of acousto-optical merit of such configuration is not as great as for the slow shear mode [9]. Currently, we have designed an innovative acousto-optical cell (AOC), based on this previously underrated material, for the frontline of information technology.

The main goal of our investigations is to reveal novel physical details inherent in the nonlinearity of a non-collinear two-phonon AOLS controlled by elastic waves of finite amplitude, to investigate features of this nonlinearity both theoretically and experimentally in wide-aperture crystals with moderate linear acoustic attenuation, and to consider an opportunity for parallel optical spectrum analysis with the significantly improved spectral resolution. Studying the local unit-level maxima in the distribution of light scattered into the second order, which appear periodically as the power density of elastic waves grows, makes it possible to identify a variety of the transfer function profiles peculiar to these maxima in the isolated planes of angular-frequency mismatches. Availability of similar maxima gives us an opportunity to choose the desirable profile for the transfer function at the fixed angle of incidence for the incoming light beam with a wide optical spectrum.

Then, we find that non-collinear two-phonon processes of AOLS are nearly 100% efficient at the fixed optical wavelength for various acoustic frequencies as well as with the fixed acoustic frequency for various optical wavelengths due to the existence of an additional dispersive birefringence factor that can be distinguished within this non-linear phenomenon. However, the first option with the fixed optical wavelength cannot be used for linear spectrum analysis of radio-wave signals principally owing to the existence of a strongly non-linear dependence between the incoming electronic signal, i.e. the acoustic waves of finite amplitude in an AOC, and the scattered light waves. In contrast, under the same conditions a dependence of the scattered light waves on the incident light is nevertheless linear within the nonlinear non-collinear two-phonon AOLS, which can also double the spectral resolution. Therefore, in view of developing a new approach to parallel spectrum analysis of wide-spectrum optical signals with significantly improved resolution, we choose the second option with the fixed acoustic frequency, see Fig. 1, which gives us an opportunity to propose a pioneer practical application of the non-collinear two-phonon AOLS for the first time to our knowledge. Generally speaking, potential spectral resolution of spectrometers exploiting the non-collinear AOC includes ordinary birefringence of a crystal as a basic parameter of the chosen material, which determines its possibilities.

In applying this new approach, we demonstrate an opportunity to replace the physically limited birefringence of a crystal by that significantly larger birefringence factor, inherent in the non-collinear two-phonon AOLS. Moreover, it can be done together with doubling the spectral

resolution, which is peculiar to the non-collinear two-phonon AOLS in principle, as shown in Fig. 1. These possibilities are demonstrated theoretically for the crystals of tetragonal symmetry as examples and confirmed during the experiments with a specially designed unique wide-aperture AOC using the calomel ($\alpha\text{-Hg}_2\text{Cl}_2$) single crystal and governed by elastic waves of finite amplitude.

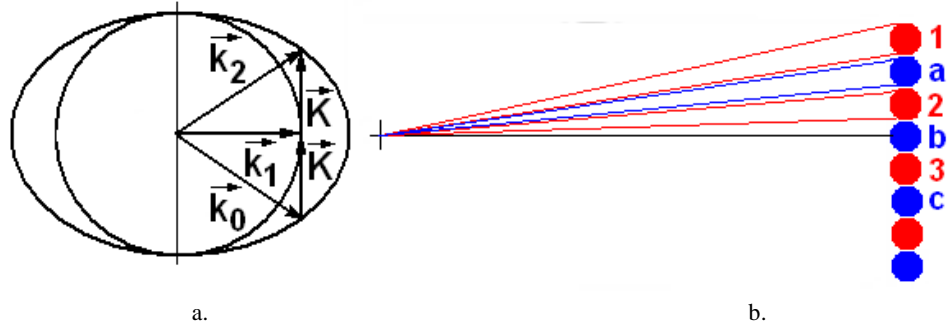


Fig. 1. The non-collinear two-phonon AOLS vector diagram: (a) and doubling the spectral resolution (b). Spots 1,2,3,... are related to one-phonon processes, while additional spots a,b,c,... describe refining the resolution caused by the appearance of a two-phonon light scattering.

2. NON-COLLINEAR TWO-PHONON AOLS GOVERNED BY ACOUSTIC WAVES OF FINITE AMPLITUDE.

Strongly nonlinear behavior of optical components with the Bragg AOLS in an anisotropic medium can be achieved easily in usual experiments without any observable influence of the scattering process on the acoustic wave. In this case the amplitude of the acoustic wave is governed by a homogeneous wave equation in so-called weak coupling regime [10]. Let us assume that the area of propagation for the acoustic wave, traveling almost perpendicularly to the light beams, is bounded by two planes $x = 0$ and $x = L$ in a uniaxial crystal, taking into account both angular and frequency mismatches in the wave vectors. Usually, the Bragg acousto-optical processes include three-waves: the incident and scattered light modes as well as an acoustic mode, and incorporates conserving both the energy and the momentum for each partial act of a one-phonon AOLS [11]. However, at certain incident angles of light shining on selected crystal cuts and at a fixed frequency of the acoustic wave, one can observe Bragg scattering of light caused by the participation of two phonons, so that the conservation laws are given by $\nu_1 = \nu_0 + f$, $\vec{k}_1 = \vec{k}_0 + \vec{K}$, $\nu_2 = \nu_0 + 2f$, and $\vec{k}_2 = \vec{k}_0 + 2\vec{K}$ simultaneously (ν_m , \vec{k}_m and f , \vec{K} are the frequencies and wave vectors of light and acoustic waves, $m = 0, 1, 2$), see Fig. 1a. Such a four-wave process occurs at the frequency f_0 of the acoustic wave, exactly peculiar to a two-phonon AOLS, which can be determined from [12]

$$f_0 = \lambda^{-1} V b, \quad (1)$$

where $b = \sqrt{|n_0^2 - n_1^2|}$ is remarkably dispersive birefringence factor and $n_0 \neq n_1$ are the current refractive indices of a crystal, V is the ultrasound velocity, λ is the incident light wavelength. The polarization of light in the zero and second orders is orthogonal to the polarization in the first order; whereas the frequencies of the light beams in the first and second orders of scattering are shifted by f_0 and $2f_0$, respectively, with reference to the zero order due to the Doppler frequency shift.

A set of equations for the complex amplitudes $C_m(x)$ of light waves ($m = 0, 1, 2$), appearing due to a quasi-stationary two-phonon Bragg AOLS governed by acoustic waves of finite amplitude, is given by [12]

$$\begin{aligned} \text{a) } \frac{dC_0}{dx} &= -\sigma C_1 \exp(-i\eta_0 x), \\ \text{b) } \frac{dC_1}{dx} &= \sigma [C_0 \exp(i\eta_0 x) - C_2 \exp(-i\eta_1 x)], \\ \text{c) } \frac{dC_2}{dx} &= \sigma C_1 \exp(i\eta_1 x), \end{aligned} \quad (2)$$

where x is the coordinate along light propagation. The combined effect of factors expressing both the acousto-optical material efficiency and the acoustic power is described by $\sigma = \pi (\lambda \cos \theta)^{-1} \sqrt{M_2 P/2}$; θ is the angle of incidence for an external plane light wave, M_2 is the

figure of acousto-optical merit, and P is the acoustic power density. A square-law nonlinearity exists that is connected to the products $C_m P^{1/2}$ on the right sides of Eq.(2). The constant angular-frequency mismatches $\eta_m = k_{m,x} - k_{m+1,x}$ are explained in terms of x-components for light wave vectors. We analyze Eq.(2) with the simplest boundary conditions $|C_0(x=0)|^2 = I$, $C_{1,2}(x=0) = 0$ and exploit the conservation law $|C_0|^2 + |C_1|^2 + |C_2|^2 = I$, resulting from Eq.(2), where I is the intensity of the incident continuous-wave light beam.

Now, we assume the precise angular alignment of the incident light and expand η_0 and η_1 into series in terms of powers of only the frequency detuning $|f - f_0|$ for the current acoustic frequency f relative to the frequency $f_0 = \Omega_0 / (2\pi)$. In the second order approximation, one can obtain from the diagram of wave vectors that $\eta_0 \approx \pi \lambda n_1^{-1} V^{-2} |f - f_0|^2$ and $\eta_1 \approx \pi \lambda n_0^{-1} V^{-2} (4 f_0 |f - f_0| + 7 |f - f_0|^2)$ [12] with $n_0 < n_1$. Therefore, in the first order approximation we may put $\eta_0 \approx 0$ and $\eta \approx \eta_1 \approx 4\pi \lambda n_0^{-1} V^{-2} f_0 |f - f_0|$. After that, one can put $S_{0,1} = C_{0,1}$, $S_2 = C_2 \exp(-i \eta x)$ and rewrite Eq.(2) as

$$\text{a) } \frac{dS_0}{dx} = -\sigma S_1, \quad \text{b) } \frac{dS_1}{dx} = \sigma (S_0 - S_2), \quad \text{c) } \frac{dS_2}{dx} = \sigma S_1 - i\eta S_2. \quad (3)$$

Now, the corresponding boundary conditions are

$$S_0(x=0) = 1, \quad S_{1,2}(x=0) = 0. \quad (4)$$

This set of the combined first-order differential equations can be converted into a triplet of equations of the third-order for complex amplitudes S_m , and these equations are independent from one another. In the case of $d\sigma/dx = 0$, these equations reduce to one describing all the light waves

$$\frac{d^3 S_m}{dx^3} + i\eta \frac{d^2 S_m}{dx^2} + 2\sigma^2 \frac{dS_m}{dx} + i\eta \sigma^2 S_m = 0. \quad (5)$$

The general solution for the complex amplitude S_2 is

$$S_2 = \frac{\sigma^2 \exp(a_1 x)}{(a_1 - a_2)(a_1 - a_3)} - \frac{\sigma^2 \exp(a_2 x)}{(a_1 - a_2)(a_2 - a_3)} + \frac{\sigma^2 \exp(a_3 x)}{a_1 a_2 - a_1 a_3 - a_2 a_3 + a_3^2}; \quad (6)$$

where a_k , ($k = 1, 2, 3$) are the roots of the characteristic equation $a^3 + i\eta a^2 + 2\sigma^2 a + i\eta \sigma^2 = 0$ for Eq.(5). This solution leads to a 3D-distribution $|C_2|^2 = |S_2(\sigma x, \eta x)|^2$, expressed in terms of 2 dimensionless parameters σx and ηx , describing the acoustic power density and the angular-frequency mismatch, respectively, see Fig. 2. This plot demonstrates a specific square-law acousto-optical nonlinearity inherent in the non-collinear two-phonon AOLS governed by elastic waves of finite amplitude. Moreover, Fig. 3 exhibits a sequence of unit-level maxima that are often desirable for potential practical applications, particularly to the spectrum analysis of optical signals. The first quartet of maxima is placed at the points $(\sigma x)_1 \approx 2.22$, $(\sigma x)_2 \approx 6.66$, $(\sigma x)_3 \approx 11.11$, and $(\sigma x)_4 \approx 15.55$. At these points, one can obtain four particular profiles in terms of the dimensionless angular-frequency mismatch ηx , see Fig. 4.

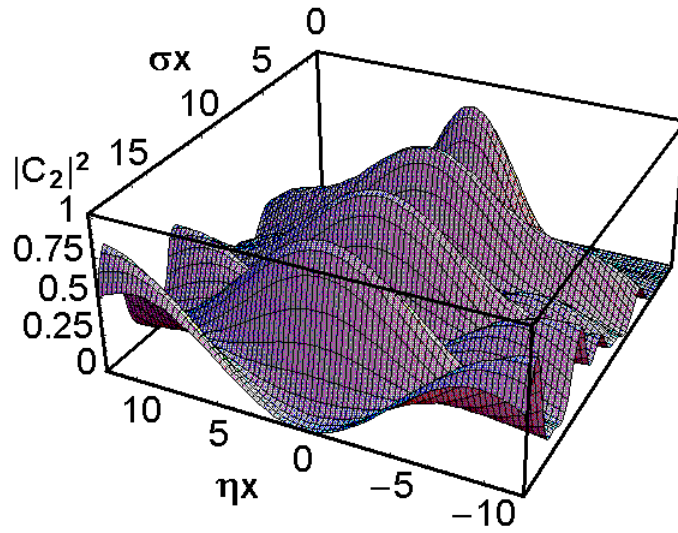


Fig. 2. A 3D-bandshape for the non-collinear two-phonon AOLS; the axis σx (the dimensionless acoustic power density) reflects nonlinearity of the phenomenon, ηx is the dimensionless angular-frequency mismatch.

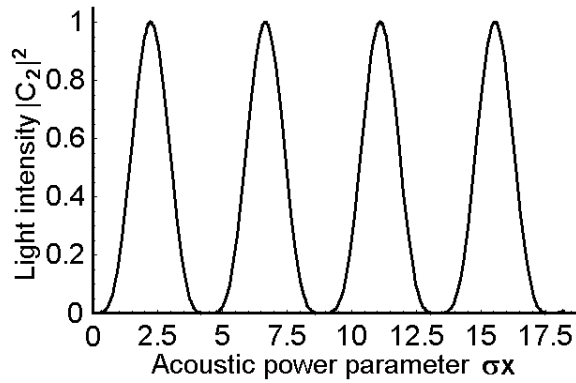


Fig. 3. Maxima of the non-collinear two-phonon AOLS reflecting its strongly non-linear behavior along the line $\eta x = 0$.

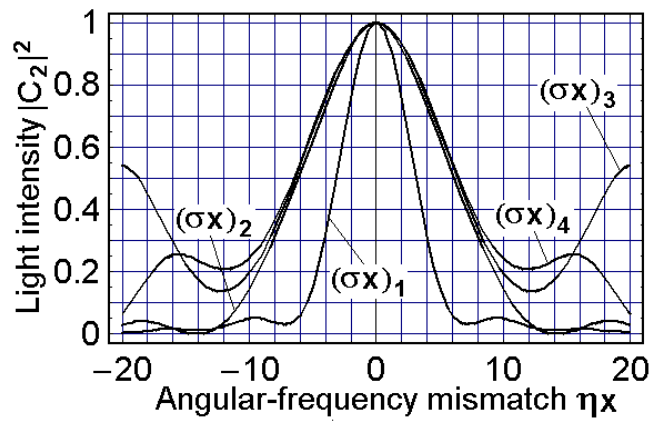


Fig. 4. The intensity – mismatch profiles related to first four maxima of the non-collinear two-phonon AOLS.

Then, plots in Fig. 4 also demonstrate an influence of specific acousto-optical square-law nonlinearity and show that the second maximum in Fig. 3 already gives close to the widest bandwidth of a two-phonon AOLS at a reasonably high acoustic power parameter $(\sigma x)_2 \approx 6.66$. Consequently, exactly this maximum with a two-side variation of the dimensionless mismatch about $\Delta\eta = (\eta x)_- + (\eta x)_+ \approx 4\pi$ at the half-maximum level can be selected as the most appropriate one for realizing a wide-bandwidth two-phonon AOLS. In the case of exact angular alignment, the mismatch η is only achieved by the frequency detuning $|f - f_0|$, so that, as it is seen directly from Eq.(2), $\eta = 2\pi |f - f_0| / V$. With $x = L$, the second profile from Fig. 4 leads to $\Delta\eta \approx 2\eta \approx 4\pi / L$, so that the frequency bandwidth for the second maximum is given by

$$\Delta f = 2 |f - f_0| \approx n_0 V^2 / (\lambda L f_0) . \quad (7)$$

Here, the length L of AOLS, the current frequency f_0 , and the optical wave length λ have to provide the Bragg regime of AOLS.

3. FREQUENCY AND LENGTH OF AN α -Hg₂Cl₂ AOC BASED ON THE NON-COLLINEAR TWO-PHONON AOLS

To make more concrete our consideration an appropriate acousto-optically effective crystalline material will be selected for further analysis. During the selection of a similar appropriate material, a few possibilities of exploiting either longitudinal L or shear S elastic modes passing along various directions had been preliminarily estimated. In particular, the subjects of our attention were the modes L[001] and S[110] in rutile (TiO₂), S[100] in lithium niobate (LiNbO₃), L[100] and S[110] in calomel (α -Hg₂Cl₂). They allow the non-collinear two-phonon AOLS and can be considered as desirable alternatives operating at rather different acoustic frequencies. The analysis has shown that the best option for further experiments, motivated by very high efficiency of AOLS and not too high acoustic frequency, is the calomel single crystal. This crystal belongs to the 4/mmm-tetragonal symmetry group, has spectral transmission band $\Delta\lambda = 0.38 - 28 \mu\text{m}$ and the material density $\rho \approx 7.2 \text{ g / cm}^3$ [13]. It has a pair of dispersive refractive indices, whose main values are $N_O = 1.9634$ and $N_E = 2.6217$ at the wavelength $\lambda = 633 \text{ nm}$. Then, in particular, this crystal allows at least two pure elastic modes, namely, the slow shear mode with the wave vector $\vec{K} \parallel [110]$, the displacement vector $\vec{u} \parallel [1\bar{1}0]$, the phase velocity $V_{SS} \approx 0.347 \times 10^5 \text{ cm/s}$, and the acoustic wave attenuation factor $\Gamma \approx 230 \text{ dB / (cm GHz}^2)$. There is also the longitudinal mode with $\vec{K} \parallel \vec{u} \parallel [100]$, $V_L \approx 1.622 \times 10^5 \text{ cm/s}$, and $\Gamma \approx 12.5 \text{ dB / (cm GHz}^2)$. It is important to note that both these elastic modes are potentially suitable for effective non-collinear two-phonon AOLS.

Now, we make the new step of studying the nonlinearity of non-collinear two-phonon AOLS, see Fig. 5. This step can be represented for the corresponding processes of scattering in terms of two surfaces for the refractive indices of ordinary (see the internal dark sphere) and extraordinary (see the external faint ellipsoid) light waves for a tetragonal crystal at the fixed optical wavelength λ (here, the calomel crystal at $\lambda = 633 \text{ nm}$ is taken as an example with $N_E \geq N_O$). The sizes of both sphere and ellipsoid will be varied depending on λ due to remarkable dispersion of the crystalline material within potential optical range. The vertical axis in Fig. 5 is oriented along the optical axis [001] of a crystal, while orientation for a pair of the horizontal axes depends on the chosen elastic modes.

For the calomel crystal, in particular, they can be taken as [110] and [11, $\bar{0}$] for the slow shear mode or as [100] and [010] for the longitudinal mode. Then, in either case, this figure includes a pair of vector diagrams illustrating two opportunities for two-phonon AOLS through various angles, which use different acoustic frequencies and birefringence factors b . Two triplets of vectors, going from the geometric center of surfaces, represent the optical wave vectors describing the corresponding orders of AOLS, whereas sequential pairs of the acoustic wave vectors reflect two-phonon processes. The upper vector diagram in Fig. 5 corresponds to smaller birefringence, i.e. to smaller factor b , and lower acoustic frequency f_0 (i.e. shorter vectors \vec{K}) than the other vector diagram depicted lower, operating by larger factor b and higher acoustic frequency f_0 (i.e. longer vectors \vec{K}). Thus these plots reflect the existence of an additional physical degree of freedom inherent in the nonlinearity of the two-phonon AOLS. This degree of freedom permits the fixed frequency f_0 to exert control over various optical wavelengths scattered through different angles.

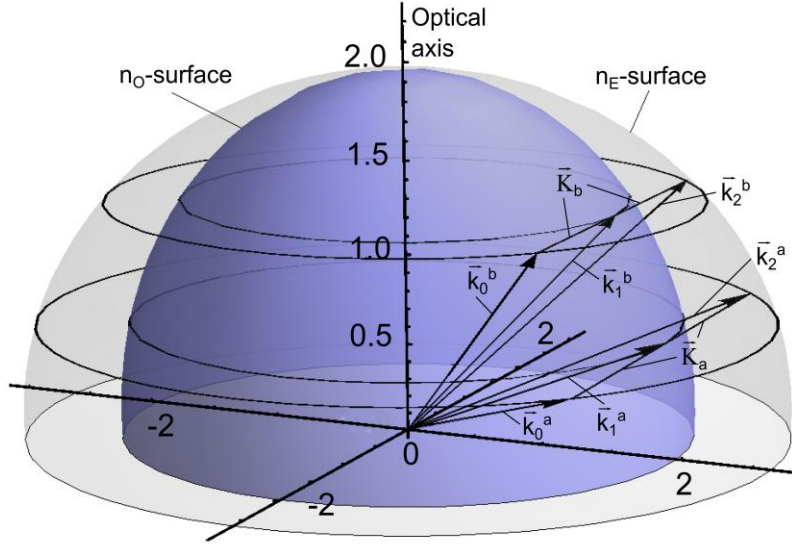


Fig. 5. Two examples of vector diagrams, indexed by “a” and “b”, inherent in nonlinear two-phonon AOLS with the fixed ratio V / λ . The extraordinary refractive index n_E is described by an external faint ellipsoid, while a darker internal sphere shows the ordinary refractive index $n_o \equiv N_o$. Here, $\vec{k}_m^{a,b}$ and $\vec{K}_{a,b}$ are the wave vectors of light and acoustic waves.

In this case, one has to consider two pairs of surfaces peculiar to the refractive indices of ordinary and extraordinary light waves for a tetragonal crystal and each similar pair of surfaces will correspond to an individual light wavelength. Nevertheless, the corresponding vector diagrams for two different nonlinear processes of two-phonon AOLS will include acoustic vectors \vec{K} of the same lengths characterizing the same acoustic frequency f_0 .

Calomel is a uniaxial crystal, so that $n_o \equiv N_o$ is the main refractive index for the ordinary state of polarization, while n_E depends on a direction in a crystal and has the form of an ellipsoid. We are interested in rather small tilts from the [001]-axis. Therefore, one can consider the angle $\psi \in [0, \pi / 2]$ of a tilt from the [001] -axis. Considering the geometry yields

$$n_E^2 = \frac{N_E^2 N_O^2 (1 + \tan^2 \psi)}{N_E^2 + N_O^2 \tan^2 \psi} \geq n_o^2 \equiv N_O^2. \quad (8)$$

Substituting Eq.(8) into Eq.(1), one can obtain

$$\psi [\text{rad}] = \arctan \left[\frac{\lambda f_0 N_E}{N_o \sqrt{V^2 (N_E^2 - N_O^2) - \lambda^2 f_0^2}} \right]. \quad (9)$$

Then, within designing an AOC based on a crystal with moderate acoustic losses and under the action of the acoustic wave of finite amplitude, the spectral resolution $\delta \lambda_0$ of potential dispersive component based on similar AOC can be estimated as

$$\delta \lambda_0 = \lambda^2 / (2b D). \quad (10)$$

This value does not include any parameters of the acoustic wave and, besides the optical aperture D , depends only on the birefringence factor b peculiar to a crystal and the incident light wavelength λ . The desirable aperture D in Eq.(10) has to be chosen to satisfy a few requirements depending on a set of various physical factors, the main one is the acoustic attenuation. If an acceptable level of acoustic losses per optical aperture D is B [dB/aperture], one can write that $D = B / (\Gamma f_0^2)$. From these formulas, one can find the denominator in Eq.(10) to be

$$2bD = \frac{2\lambda B}{V\Gamma f_0^2} . \quad (11)$$

Restricting ourselves to the level $B \equiv 6\text{dB/aperture}$ and using the above-mentioned data for the two chosen pure elastic modes in calomel, one can obtain for $\lambda = 405\text{ nm}$ and 633 nm (see in the following plots shown in Figs.6 and 7).

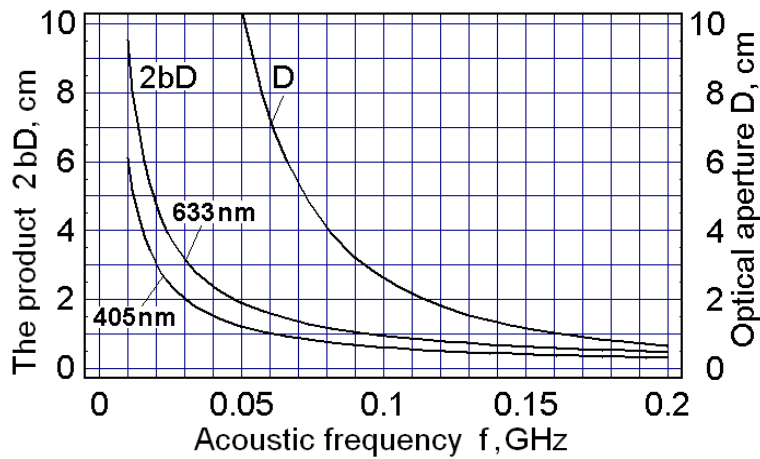


Fig. 6. The product $2bD$ and the desirable aperture D , connected with the spectral resolution, for the slow shear elastic mode in calomel.

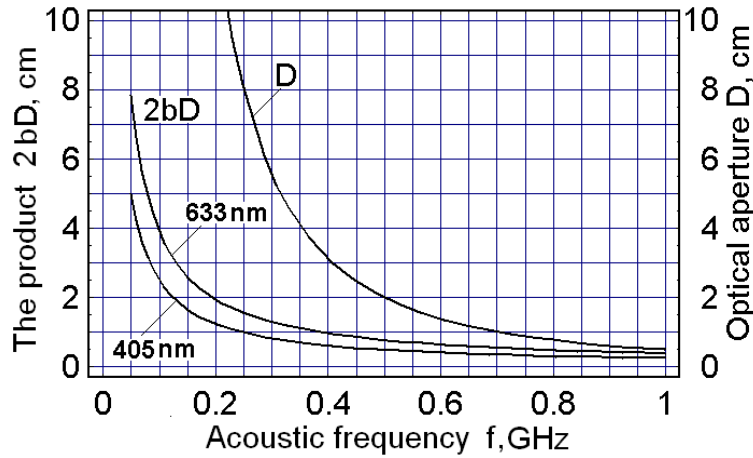


Fig. 7. The product $2bD$ and the desirable aperture D , connected with the spectral resolution, for the longitudinal elastic mode in calomel.

Before we analyze these diagrams further, we motivate the above-taken selection of the level $B = 6$ dB for acoustic losses per optical aperture. As such, we attempt to describe shaping the resolvable spot after an AOC in a spectrum analyzer. The normalized distribution $I(u)$ of light intensity of that individual resolvable spot is given by

$$I(u, \alpha_0) = \frac{\sin^2(\pi u) + \sinh^2(\alpha_0/2)}{[1 + (2\pi u/\alpha_0)^2] \sinh^2(\alpha_0/2)}, \quad (12)$$

where $u = w D / \lambda F$; w is the physical spatial coordinate in the focal plane, F is the focal distance of the integrating lens, and $\alpha_0 = \alpha D$ is the acoustic loss factor per aperture. Analysis of Eq.12 shows that $\alpha_0 \equiv B = 6$ dB / aperture gives the first zero in the distribution $I(u)$ at a level about -20 dB. Choosing $B = 6$ dB allows us to avoid unnecessarily strong limitations for this stage of studies. Together with this, the main lobe in the distribution $I(u)$ will be almost no widened at $B = 6$ dB / aperture.

4. EFFICIENCY OF THE NON-COLLINEAR TWO-PHONON AOLS IN A-Hg₂Cl₂ UNIAXIAL CRYSTAL.

Obtaining the figure of acousto-optical merit M_2 inherent in the selected cut of an α -Hg₂Cl₂ crystal first requires finding the effective photo-elastic constant p_{eff} . To do so, keep in mind that each dynamic acoustic grating can be characterized by its symmetric deformation tensor of the second rank $\gamma = (\bar{u} \cdot \bar{q} + \bar{q} \cdot \bar{u})/2$, where $\bar{q} = \bar{K}/|K|$ is the unit vector of the wave normal.

4.1. The case of the slow shear elastic mode with $\bar{K} \parallel [110]$, $\bar{u} \parallel [1\bar{1}0]$

Due to $\bar{q} = (1,1,0)/\sqrt{2}$ and the normalized displacement vector is $\bar{u} = (1,-1,0)/\sqrt{2}$, the corresponding deformation tensor takes the following dyadic form

$$\gamma^{(S)} = 0.5 \{(\bar{x}_1 \bullet \bar{x}_1) - (\bar{x}_2 \bullet \bar{x}_2)\} \quad (13)$$

The tensor $\gamma^{(S)}$ of the second rank with the components $\gamma_{kl}^{(S)}$ ($k, l = 1, 2, 3$) in the basis $(\bar{x}_1, \bar{x}_2, \bar{x}_3)$ can be converted into a 6-dimension vector $\bar{\gamma}^{(S)} = (1, -1, 0, 0, 0, 0)$ [14]. To estimate the efficiency of AOLS associated with the above selected slow shear acoustic mode, the photo-elastic tensor p of the fourth rank should be converted into the form of a 6×6 matrix with the components $p_{\lambda\mu}$. For α -Hg₂Cl₂ (4/mmm), the matrix representation for the tensor p gives the following non-zero components: $p_{11} = p_{22} = 0.551$, $p_{12} = p_{21} = 0.44$, $p_{13} = p_{23} = 0.256$, $p_{31} = p_{32} = 0.137$, $p_{33} = 0.1$, $p_{44} = p_{55}$ - unknown, and $p_{66} = 0.047$ at $\lambda = 633$ nm [15]. Now, one can calculate the matrix product $p\bar{\gamma}^{(S)} = 0.5(p_{11} - p_{12})(1, -1, 0, 0, 0, 0)$ and convert it back to the form of a standard tensor ($p\gamma^{(S)}$) of the second rank [14]. The effective photo-elastic constant can be written from the scalar form $p_{\text{eff}}^{(S)} = \bar{e}_1(p\gamma^{(S)})\bar{e}_0$; i. e.

$$p_{\text{eff}}^{(S)} = 0.5(p_{11} - p_{12}) \bar{e}_1 [(\bar{x}_1 \bullet \bar{x}_1) - (\bar{x}_2 \bullet \bar{x}_2)] \bar{e}_0, \quad (14)$$

where the vectors \bar{e}_0 and \bar{e}_1 usually describe the polarization states of incident and scattered light beams, respectively. Within the anomalous non-collinear AOLS the eigen polarization vectors \bar{e}_0 and \bar{e}_1 of the incident and scattered light beams should be orthogonal to one another $\bar{e}_0 \perp \bar{e}_1$, and they both should also be lying in the same plane as the wave vector $\bar{K} \parallel [110]$.

For the sake of simplicity, in this case, one can take $\bar{e}_0 \parallel \bar{K}$ and $\bar{e}_1 \parallel \bar{u}$, i.e. $\bar{e}_0 = (1,1,0)/\sqrt{2}$ and $\bar{e}_1 = (1,-1,0)/\sqrt{2}$. Then, one can obtain $(p\gamma^{(S)}) \cdot \bar{e}_0 = 2^{3/2}(p_{11} - p_{12})(1, -1, 0)$ and find

$$p_{\text{eff}}^{(S)} = \bar{e}_1(p\gamma^{(S)})\bar{e}_0 = 0.5(p_{11} - p_{12}) \approx 0.055 \quad (15)$$

The corresponding figure of acousto-optical merit M_2 also depends on the material density $\rho = 7.2$ g/cm³ and a pair of rather dispersive refractive indices. Using, for instance, $n_O = 1.9634$ and $n_E = 2.6217$ at $\lambda = 633$ nm, one can find $M_2^{(S)} = n_O^3 n_E^3 (p_{\text{effmax}}^{(S)})^2 / (\rho V_{SS}^3) \approx 1371 \times 10^{-18}$ s³/g. This value

demonstrates that the anomalous regime of AOLS governed by the pure slow shear acoustic mode in the calomel single crystal is very efficient and is able to provide an effective two-phonon AOLS.

4.2. The case of the longitudinal elastic mode with $\vec{K} \parallel \vec{u} \parallel [100]$

Exploiting the above described procedure with $\vec{q} = \vec{u} = (1,0,0)$, one can obtain a 6-dimension vector $\vec{\gamma}^{(L)} = (1,0,0,0,0,0)$ and then find $p\vec{\gamma}^{(L)} = (p_{11}, p_{21}, p_{31}, 0,0,0)$ [14] with $p_{11} = 0.551$, $p_{21} = 0.44$, and $p_{31} = 0.137$. Consequently, the effective photo-elastic constant can be expressed as $p_{eff}^{(L)} = \vec{e}_1 (p\gamma^{(L)}) \vec{e}_0$, i. e.

$$p_{eff}^{(L)} = \vec{e}_1 \{ p_{11}(\vec{x}_1 \bullet \vec{x}_1) + p_{21}(\vec{x}_2 \bullet \vec{x}_2) + p_{31}(\vec{x}_3 \bullet \vec{x}_3) \} \vec{e}_0, \quad (16)$$

where as before the vectors \vec{e}_0 and \vec{e}_1 describe the polarization states of incident and scattered light beams, respectively. Then they should be orthogonal to one another $\vec{e}_0 \perp \vec{e}_1$ and lying in the plane that includes the wave vector $\vec{K} \parallel [100]$. Because of $p_{21} > p_{31}$, the most attractive option appears via choosing $\vec{e}_{0,1} \in (010)$ with $\vec{e}_0 = (\cos \alpha, \sin \alpha, 0)$ and $\vec{e}_1 = (-\sin \alpha, 0, \cos \alpha)$, where α is an angle between vectors \vec{e}_0 and $\vec{K} \parallel [100]$. Such a choice leads to

$$p_{eff}^{(L)} = \vec{e}_1 (p\gamma^{(L)}) \vec{e}_0 = -0.5 (p_{11} - p_{13}) \sin (2\alpha). \quad (17)$$

With $\alpha = \pi / 4$ one will have $p_{effmax}^{(L)} = - (p_{11} - p_{13}) / 2 \approx -0.207$. Consequently, using the above-mentioned data, one can estimate $M_2^{(L)} = n_o^3 n_e^3 (p_{effmax}^{(L)})^2 / (\rho V_L^3) \approx 190.2 \times 10^{-18} \text{ s}^3/\text{g}$. These calculations show that the anomalous regime of AOLS controlled by the pure longitudinal elastic mode is also efficient and can be used to realize a sufficiently effective non-collinear two-phonon AOLS in calomel as well.

5. THEORETICAL ESTIMATIONS OF A DISPERSIVE COMPONENT BASED ON THE CALOMEL-MADE CRYSTALLINE AOC

Now using the above-obtained data, the plots in Figs.6 and 7 allow us to estimate potential performances for a dispersive component based on the calomel-made crystalline AOC with the optical aperture $D = 10$ cm.

5.1. Realizing the Bragg regime of a two-phonon AOLS

The length L of Bragg AOLS in a crystal is restricted by the following inequality for Klein-Cook parameter $Q = 2\pi \lambda L f_0^2 / (n_0 V^2) \gg 1$ [16]. In calomel, for the slow shear mode passing along the [110]-axis with $V_{SS} = 0.347 \times 10^5$ cm/s, $f_0^{(S)} = \sqrt{B/(D\Gamma_S)} \approx 51.075$ MHz, and $n_0 = 2.0826$ at $\lambda=405$ nm, one finds that $L_{\min}^{(S)} \gg 0.0038$ Q cm. Taking $Q = 4\pi$, one yields $L_{\min}^{(S)} \geq 0.05$ cm and can take $L_{\min}^{(S)} \approx 0.2$ cm with a safety margin. For the pure longitudinal mode passing along the [100]-axis with $V_L = 1.622 \times 10^5$ cm/s, $f_0^{(L)} = \sqrt{B/(D\Gamma_L)} \approx 219.1$ MHz, and $n_0 = 2.0826$ at $\lambda=405$ nm, one can find $L_{\min}^{(L)} \gg 0.0045$ Q cm, so that the minimal interaction length can be so small that one can use the previous estimation of $L_{\min} \approx 0.2$ cm.

5.2. Effect of the acoustic beam divergence

The angular divergence of the acoustic beam can be considered via estimating the length X of Fresnel acoustic zone when the unknown radiating acoustic aperture is equal to R . These values are connected with one another as $X = R^2 f / (2V)$ [17]. If it is granted that the acoustic beam belongs to Fresnel acoustic zone and $X = 10$ cm, one find for α -Hg₂Cl₂ that $R \approx \sqrt{2V_S X / f_S} = \sqrt{2V_L X / f_L} \approx 0.12$ cm. Thus with $R \geq 0.15$ cm, which lies in frames of the above-agreed value and is rather typical value in practice, one can say that potential angular divergence of acoustic beam is small enough to be definitely omitted, so that the plane-wave approximation is rather close to the reality.

5.3. General estimations for the calomel-made AOC

At first, let us perform theoretical estimations for the calomel-made AOC with $D = 10$ cm and $L_{\min} \approx 0.2$ cm. The summary of similar estimations is presented in Tables 1 and 2. One can see from these tables that the highest spectral resolution and the largest number of resolvable spots within the widest spectral range can be achieved in calomel with the exploitation of the pure slow shear elastic mode.

Table 1. Theoretical estimations; here, $\delta f = V / 2D$ and $\delta\lambda = \delta f \lambda / f_0$ are frequency and spectral resolutions, $f_0 = \sqrt{B/(D\Gamma)}$ is the central acoustic frequency, and the product $2bD = \lambda^2 / \delta\lambda$ includes the birefringence factor

Wavelength λ , nm	n_0	Elastic mode	V , 10^5 cm/s	Γ , dB/(cm GHz ²)	δf , kHz	f_0 , MHz	$\delta\lambda$, Å	$2bD$, cm
405	2.0826	S[110]	0.347	230	1.735	51.08	0.1376	1.192
		L[100]	1.622	12.5	8.11	219.1	0.150	1.0935
633	1.9634	S[110]	0.347	230	1.735	51.08	0.2151	1.863
		L[100]	1.622	12.5	8.11	219.1	0.234	1.7094

Table 2. Practical estimations; here, $\Delta f = 2 |f - f_0| \approx n_0 V^2 / (\lambda L f_0)$ and $\Delta \lambda = \Delta f \lambda / f_0$ are frequency and spectral bandwidths, while $N = \Delta f / \delta f = \Delta \lambda / \delta \lambda$ is the number of resolvable spots.

Wavelength λ , nm	n_o	Elastic mode	Δf , MHz	$\Delta \lambda$, Å	N, spots
405	2.0826	S[110]	6.07	482	3500
		L[100]	30.877	571	3807
633	1.9634	S[110]	3.66	454	2110
		L[100]	18.630	538	2300

To compare these results with the collinear AOF based on a long-aperture $L = 10$ cm lithium niobate (LiNbO_3) crystal, for example, at $\lambda = 633$ nm. We choose this wavelength to avoid well-known possible problems with the effect of photorefraction in this crystal, which has $N_o = 2.28646$, $N_E \approx 2.20222$, and $|\Delta n| \approx 0.08424$ at $\lambda = 633$ nm. Then, one has to take into account that the collinear AOLS does not exhibit the above-discussed degree of freedom given by Eq.(1). As a result, it is able to give exactly one resolvable spot, i.e. to provide only sequential optical spectrum analysis. Within the collinear light scattering, the optical wavelength λ and the corresponding acoustic wave frequency are unambiguously connected. Therefore for $\lambda = 633$ nm, it requires $f = |\Delta n|V / \lambda \approx 0.8743$ GHz for pure longitudinal elastic mode with $\vec{k} \parallel [100]$ in the lithium niobate crystal has $V_L \approx 6.57 \times 10^5$ cm/s and $\Gamma \approx 0.15$ dB / (cm GHz²) [1]. This is why one can find that optical aperture or, equivalently in the collinear case, the length of AOLS is $L = B / (\Gamma f_0^2) \approx 40$ cm with $B = 6$ dB / aperture. Of course, such a length of a crystal is unachievable in practice, due to technological limitations; and one has to take $L \leq 10$ cm. In this case, one can estimate that $|\Delta n|L \approx 0.842$ cm and $\delta \lambda^{(L)} = \lambda^2 / (|\Delta n|L) \approx 0.473$ Å. This result can be marked like an individual level (or a point) on both the diagrams in Figs.6 and 7. By the way, this comparison shows that developing a new approach to optical spectrum analysis is possible. Thus we propose a parallel algorithm of signal processing with an appreciably improved spectral resolution.

6. PROOF-OF-PRINCIPAL EXPERIMENTAL DATA

6.1. Experiment arrangement

First, one can estimate the potential contributions of the acoustic losses. For the chosen slow shear elastic mode passing along the [110]-axis, whose displacement vector is oriented along the [11, $\bar{0}$]-axis. The coefficient of linear attenuation is $\Gamma \approx 230$ dB/(cm GHz²) in a calomel single crystal [15]. The factor α [cm⁻¹] of the amplitude acoustic losses is α [cm⁻¹] = 0.1152 Γ [dB/(cm GHz²)] f^2 [GHz]. The carrier frequency, peculiar to the non-collinear two-phonon AOLS in calomel, can be calculated as $f_0 \approx 71$ MHz at the above-chosen light wavelength 405 nm. Consequently, one can estimate the amplitude factors for acoustic losses by $\gamma = \Gamma f_0^2 \approx 1.16$ dB / cm and $\alpha = 0.134$ cm⁻¹.

The angular divergence of the acoustic beam in the calomel non-collinear AOC at the frequency $f_0 \approx 71$ MHz can be estimated as well. A reliable spatial size of the initial acoustic beam aperture that we will consider is close to $L \approx 0.2$ cm. With $V_{SS} = 0.347 \times 10^5$ cm/s, one can calculate the corresponding acoustic wavelength $\Lambda = V / f_0 = 0.489 \times 10^{-3}$ cm and the angle of acoustic beam divergence $\varphi = \Lambda / L \approx 0.244 \times 10^{-2}$ rad $\approx 0.14^\circ$ to conclude that the angular divergence of the acoustic beam can be omitted.

Now, we are ready to perform the few important numerical estimations inherent in the non-collinear light scattering at the light wavelength of $\lambda = 405$ nm in the calomel crystalline cell with $M_2 \approx 2546 \times 10^{-18}$ s³ / g and $L = 0.2$ cm. The periodicity of the unit-level AOLS maxima (see Fig. 3) gives us an opportunity to choose the second maximum with one of the widest bandshape at $(\sigma x)_2 \approx 6.667$, so that putting $x \equiv L$, one can find $\sigma_2 \approx 33.3$ cm⁻¹. Using the standard determination for σ [18] with $\cos \theta \approx 1$, one can write

$$P \approx \frac{2\lambda^2 \sigma^2}{\pi^2 M_2} . \quad (18)$$

Consequently, at $\lambda = 405$ nm Eq.(18) gives $P_2 \approx 145$ mW/mm² for the second maximum. Additionally, one has to take into account the losses needed for converting the electronic signal into an acoustic one, which are in practice close to 2 – 3 dB as the case requires. Usually, we have to restrict ourselves to a maximum level $P \leq 0.5$ W/mm² of acoustic power density. This requires the absolute acoustic power magnitude of about 2 W and the acoustic beam cross section of about 4 mm² in the AOC under consideration. The produced estimations demonstrate that the above-obtained level for P_2 lies in the ranges of accessible value, while similar parameters P_2 and σ_2 for the second unit-level AOLS maximum are beyond these frames. One can see from Fig. 3 that reaching the next maximum needs a much higher acoustic power density in comparison with the second one. This looks rather conjectural from the viewpoint of requirements for the electric strength inherent in the available piezoelectric transducer. After that, pre-experimental estimations for the calomel-made AOC with $D = 5.2$ cm and $L_{\min} \approx 0.2$ cm can be summarized in Table 3.

Table 3. Pre-experimental estimations; here, $d_s = \lambda F / D$ is an ideal spot size in the approximation of geometric frequency, M_2 is the figure of acousto-optical merit, and P_2 is the acoustic power density needed for the second maxima.

λ , nm	n_o	n_E	d_s , μm	δf , kHz	M_2 , s ³ / g	$\delta\lambda$, \AA	2 b D, cm	P_2 , mW / mm ²
405	2.0826	3.0379	6.620	3.337	2.5 10(-15)	0.190	0.862	145
633	1.9634	2.6217	10.347	3.337	1.4 10(-15)	0.368	1.347	657

These estimations exploit the pure slow shear elastic mode with the acoustic velocity $V_{SS} = 0.347 \times 10^5$ cm/s in the scheme of the standard acousto-optical spectrum analyzer with the integrating lens of the focal distance $F = 85$ cm.

The design of the calomel crystalline AOC under consideration, operating in the regime of the non-collinear two-phonon AOLS, is presented in detail in Fig. 8. The piezoelectric transducer represented by a thin plate made of the 163° Y-cut LiNbO₃ single crystal had been placed on the (110) crystallographic plane of the calomel crystal and provided the slow shear mode acoustic beam cross section of about 4 mm^2 at the length $L = 0.2$ cm of AOLS in calomel.

At $\lambda = 405$ nm and the above-estimated acoustic wavelength $\Lambda = 0.489 \times 10^{-3}$ cm, one can find the Bragg angle θ_0 (see Fig. 8a) needed for the non-collinear two-phonon AOLS as $\theta_0 \approx 0.0414$ rad $\approx 2.37^\circ$. Together with this, the tilt angle ψ needed for $D = 5.2$ cm and $f_0 \approx 71$ MHz (see Fig. 8b) can be estimated from Eq.(9) by the value $\psi \approx 0.0546$ rad $\approx 3.13^\circ$ with $\lambda = 405$ nm, $V_{SS} = 0.347 \times 10^5$ cm/s, $N_O = 2.0826$, and $N_E = 3.03794$ in calomel. Our proof-of-principal experiments had been performed with the specially designed wide-aperture AOC based on the unique calomel single crystal. This pioneer AOC works at optical wavelength $\lambda = 405$ nm, which combines the convenience of operating in just the visible range with the best-expected optical performances inherent in this AOC with violet light, from the single frequency solid-state laser CL-405-050--S (CrystaLaser). Theoretically (see section 5), the calomel-based AOC could be governed by the radio-wave signals whose the best acoustic performances were expected at the central frequency about 71 MHz, frequency bandwidth $\Delta f \approx 4.36$ MHz, and frequency resolution $\delta f \approx 3.337$ KHz providing the number $N \approx 1307$ of resolvable spots. The experiments included a Glan-Thompson linear polarizer and a four-prism beam expander, which operated with the light beam polarized in the plane of expanding and provided rather flat (non-uniformity $\sim 11\%$) optical beam profile. During the experiments with the beam shaper rather accurate angular adjusting of the incident light beam had been achieved. By this it means that both the correct Bragg angle of incidence and the needed tilt angle had been optimized. The 3-inch achromatic doublet lens (#30-976, Edmund Optics) with the focal length of about 85 cm had been used as the integrating lens, and the multi-pixel CCD-linear array consisting of $4.7 \mu\text{m}$ pixels was playing the role of a photo-detector. The layout of the optical scheme of the experiments is presented in Fig. 9.

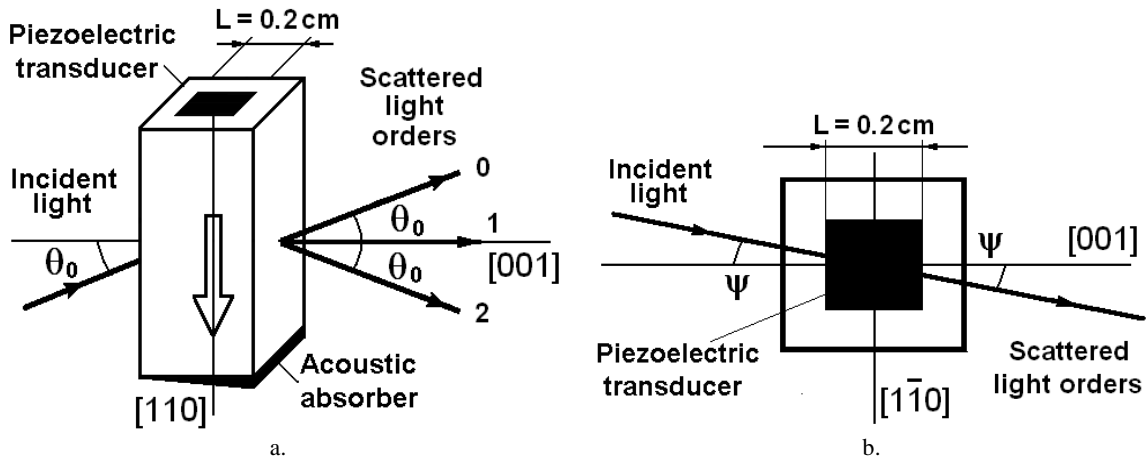


Fig. 8. The design of the calomel AOC: (a) depicts the general view with the Bragg angles of incidence and scattering in three orders, while (b) shows the top view with the needed tilt angle ψ .

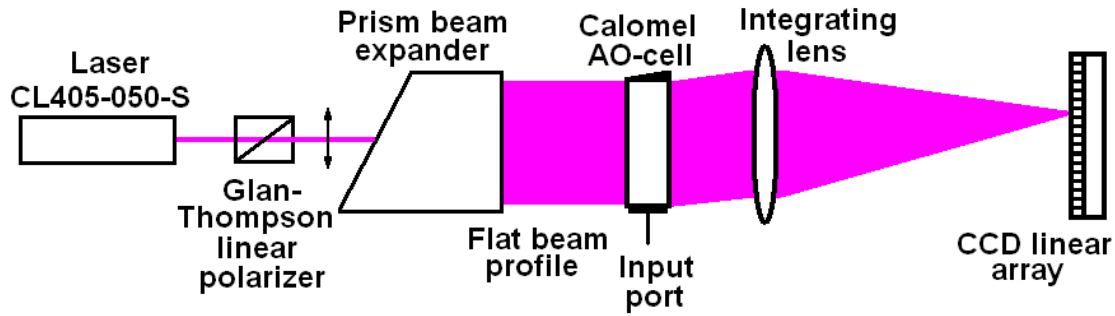


Fig. 9. The layout of the optical scheme; only the 2-nd order of a two-phonon AOLS is shown.

6.2. Experimental results

Experimental verification of the optical spectrum analysis under proposal had been carried out with the Bragg cell, made of a unique calomel ($\alpha\text{-Hg}_2\text{Cl}_2$) single crystal, which had an active optical aperture of about 52×2 mm, see Fig. 8. While operating at the optical wavelengths of 405 nm with linear state of the incident light polarization oriented along the crystallographic axis [110] on the central acoustic frequency of about 71 MHz, this cell allowed a maximum input acoustic power of about 1.5 W.

The experiments consisted of two parts. The first part included measuring the bandwidth of the Bragg non-collinear two-phonon AOLS. The second part of our experiments was related to estimating possible spectral resolution within involving this AOC into the optical spectrum analysis via measurements of the light intensity distributions peculiar to an individual spots in the focal plane of the integrating lens for light deflected by that calomel AOC into the second order. Fig. 10 shows the experimental plot for the frequency bandshape inherent in the calomel cell. One can observe the characteristic variations of efficiency at the top of the experimental plot. The total experimental frequency bandwidth at a -3 dB-level has been estimated by $\Delta f_{\text{exp}} \approx 5.1$ MHz.

The calomel crystal is very effective, but rather specific material whose transmission optical range is starting from 380 nm, while its main refractive indices are high enough and equal to about $N_o = 2.083$ and $N_e = 3.038$ at 405 nm. By this it means that one can expect remarkable optical losses and reflections with operating at 405 nm. Consequently, to optimize the experimental conditions both the input and output facets of the calomel-made acousto-optical cell should have anti-reflection coating. However, during our proof-of-principle experiments the cell had not been coated.

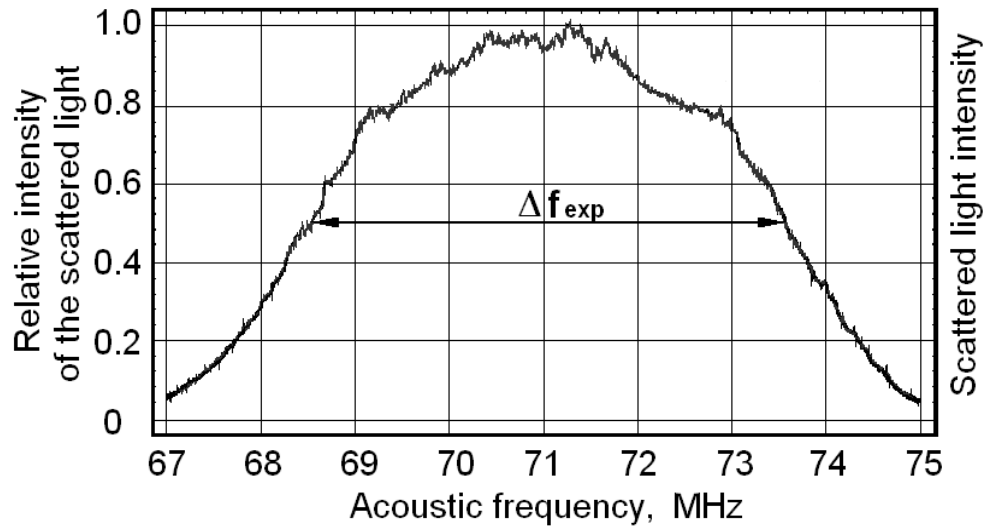


Fig. 10. Experimentally obtained frequency bandshape for the AOC made of calomel. The full width at the half-maximum level can be estimated by about of $\Delta f_{\text{exp}} \approx 5.1$ MHz.

This is why the diffraction efficiency had been estimated in terms of the transmitted light, i.e. at the output facet of the calomel-made acousto-optical cell. By this it means that the measured light intensity, transmitted through the cell without any input electronic signal at the piezoelectric transducer, had been taken to be the unity. When the input signal is applied to the piezoelectric transducer, one can measure the portion of light intensity scattered into the second order and estimate its ratio to the initially measured transmitted light intensity. Just this ratio, completely caused by an external signal, we consider as the measure of the “diffraction efficiency”. This experimentally obtained maximal ratio (i.e. the diffraction efficiency) at the optimal acoustic frequency about 71 MHz had been estimated by the value ~ 0.94 when the applied electronic signal power was about 1.2 W providing the acoustic power density ≤ 150 mW/mm².

Precise optical measurements had been performed at the wavelength 405 nm to obtain sufficiently reliable estimations for the frequency resolution providing by the α -Hg₂Cl₂-cell together with the above-described optical system, including the CCD linear array. The realized measurement had been done in the regime of the so-called “hot cell”, i.e. with a radio-wave signal applied at the input port of the α -Hg₂Cl₂-cell. Figure 11 depicts the light intensity profile with the spot size of about 8.2 microns and the side lobe level of about 6.2%, which includes affecting the light distribution in a spot by the acoustic losses of 6 dB / aperture. This plot is a result of the standard computer processing realized by the CCD-camera. The produced measurements showed that the main lobe of a partial optical beam gave the spot size lighting almost two pixels of the CCD-row that provided rather acceptable resolution of a pattern from viewpoint of the sampling theorem.

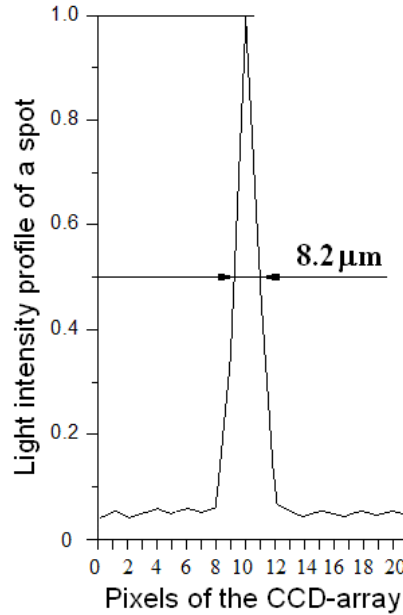


Fig. 11. Light intensity profile of an individual resolvable spot observed in the 2nd order of scattering. It is a result of the standard processing provided by the CCD-camera. The full width at the half-maximum of the main lobe can be estimated by about of 8.2 microns.

As it had been noted, our experimental results have been obtained using the integrating lens with $F = 85$ cm at the wavelength 405 nm, so that theoretically the spot size is $d_s = \lambda F / D \approx 6.62 \mu\text{m}$. Together with this, the plot in Fig. 11 exhibits the experimental spot size $d_T = \lambda F / D_T \approx 8.2 \mu\text{m}$ that corresponds to the aberration factor $\zeta_T \approx 1.2375$ (which includes, of course, optical imperfectness of the system), and consequently, to the effective aperture $D_T \approx 4.202$ cm for the AOC. The last data show that about 20% of the active optical aperture of the AOC is lost due to imperfectness of the lens and cell's material. Therefore, instead of theoretical limit of the frequency resolution $\delta f = V / 2D \approx 3.337$ kHz, one yields the measured value $\delta f_T = V / 2D_T \approx 4.13$ kHz. Then, $\Delta\lambda_T = \Delta f_T \lambda / f_0 \approx 291 \text{ \AA}$ (instead of the theoretical value $\Delta\lambda \approx 248.7 \text{ \AA}$) with $\delta\lambda_T = \lambda \delta f_T / f_0 \approx 0.235 \text{ \AA}$. Thus the experimentally obtained number of resolvable spots is $N_T = \Delta f_T / \delta f_T = \Delta\lambda_T / \delta\lambda_T \approx 1235$ spots, which is rather close to the obtained theoretical estimation. Finally, the expected lighted length in the focal plane of the integrating lens is $L_{CE} = d_T N_T \approx 10.12$ mm, i.e. capabilities of the experimental optical system lie in the frames of the exploited multi-pixel CCD-array.

The obtained results with calomel AOF (the spectral resolution $\delta\lambda \approx 0.235 \text{ \AA}$ at 405 nm, which gives the resolving power $R \approx 17,200$) can be compared with the most advanced to our knowledge, acousto-optical spectrometers for space or airborne operations of the twenty-first century. For example, one can mention astrophysically oriented acousto-optical spectrophotometer, exploiting a TeO_2 based AOF, exhibited the spectral resolution $\delta\lambda \approx 12 \text{ \AA}$ at $\lambda = 636.5$ nm [19], then the acousto-optical spectrometers used onboard space mission Mars Express with $\delta\lambda \approx 5 \text{ \AA}$ at $\lambda \approx 1000$ nm [20] and space mission Venus Express with $\delta\lambda \approx 4.2 \text{ \AA}$ at $\lambda \approx 650$ nm [21]. Also, we can compare our results with previously mentioned KDP AOF, which exhibits a high spectral resolution $\delta\lambda \approx 0.625 \text{ \AA}$ at $\lambda \approx 325$ nm giving the resolving power $R \approx 5,200$ [5]. Together with this, one can take the other data from our introduction. By this it means that our results with calomel AOF can be considered like the best we can mention at the moment.

7. CONCLUSION

We have revealed novel physical aspects peculiar to square-law nonlinearity of the non-collinear two-phonon AOLS governed by elastic waves of finite amplitude in birefringent crystals. This phenomenon manifests rather specific parametric nonlinearity within AOLS, which can be observed at reasonable level of acoustic power density in some anisotropic materials exhibiting moderate linear acoustic losses. First, strongly nonlinear behavior of both the transmitted light intensity and the angular-frequency mismatch had been distinguished. Then, these characteristics had been studied theoretically. A sequence of the local unit-level maxima and a variety of the transfer function profiles peculiar to these maxima in the distribution of light scattered into the second order had been identified and considered. As a result, the second unit-level maximum, providing one of the widest profiles for the transfer function, had been selected. Potential application of this profile is related to a unique option for the precise spectrum analysis of optical signals. The criterion for similar selection was based on the above-mentioned combination of achieving already sufficiently wide transfer function and exploiting the unit-level maximum in the non-collinear two-phonon AOLS distribution that requires still not too high acoustic power density for manifesting that square-law nonlinearity. Then, we have found, identified, and characterized an additional degree of freedom related to the non-collinear two-phonon AOLS, which means the following possibility. Namely, the two-phonon processes allow close to 100% efficiency with the fixed optical wavelength for various acoustic frequencies as well as with the fixed acoustic frequency for various optical wavelengths due to existence of an additional dispersive birefringence factor inherent in this phenomenon, see Fig. 5. Because of the interplay between the scattered light waves and the incident ones is linear in behavior in spite of strong acousto-optical non-linearity peculiar to the non-collinear two-phonon AOLS, we have chosen this effect to apply it to realize an advanced optical spectrum analysis with the doubled accuracy. By this it means that the second possibility, namely, the case with the fixed acoustic frequency for various optical wavelengths, had been taken in a view of developing a new approach to the parallel spectrum analysis of optical signals. Moreover, due to two-phonon processes give doubling the spectral resolution in the acousto-optics, the spectrum analysis of optical signals with the significantly improved resolution has been obtained as well.

Usually, the spectral resolution of, for example, collinear tunable acousto-optical filter depends on the birefringence of the exploited crystal, which is fixed as a basic parameter of the chosen material. The approach under proposal makes it possible to replace that physically limited and the fixed birefringence of a crystal by the new relatively larger birefringence factor, inherent in square-law nonlinearity of the non-collinear two-phonon AOLS. Moreover, this factor of birefringence can be varied through choosing the above-described tilt angle whose acceptability depends on the symmetry of a crystal. In these circumstances, already only the acoustic attenuation plays the role of a limiting factor, which restricts potential performances of spectrum analysis. In our case, a 6-dB level of the acoustical losses per optical aperture of the AOC had been motivated and taken to avoid unnecessary strong limitations during the current stage of investigations.

To demonstrate the details of our analysis and to realize possible experiments the crystals of tetragonal symmetry had been considered as examples. Then, very effective acousto-optical material, i.e. the calomel (α -Hg₂Cl₂) single crystal had been selected as one of the best options for our goals. The needed theoretical, practical, and pre-experimental estimations had been performed to design a really unique wide-aperture AOC based on the calomel crystal. The experiment had been carried out at $\lambda = 405$ nm with a 5.2 cm aperture AOC made of calomel excited by the slow shear acoustic mode along the [110]-axis. Along with this, we had explored the use of rather

specific directions for the optical waves in order to select adequate refractive indices within the AOLS. The results of the performed proof-of-principal experiments with this AOC, governed by elastic waves of finite amplitude, confirm in general the previously developed theoretical analysis and numerical estimations. Moreover, these results open the way to the application of the proposed innovative technique to an advanced optical spectrum analysis with the radically improved spectral resolution.

ACKNOWLEDGEMENTS

The authors would like to thank Dr. William F. Wall (INAOE) for the detailed discussion of this article and for his assistance within the preparation of our manuscript. The work was supported by CONACyT, project # 61237 (initially) and AdlOptica GmbH (Berlin, Germany).

REFERENCES

1. N. Uchida and N. Niizeki, "Acoustooptic deflection materials and techniques", Proc. IEEE, Vol. 61, No. 8, 1073-1092, (1973).
2. L. Wei, S. Yu-Nan, C. Fang, & B. Long, "Feasibility of Non-Collinear TeO₂ Acoustic-Optic Tunable Filters Used in the Optical Communication", Chinese Physics Letters, 24(4), 986-989, (2007).
3. Catalog of Acousto-Optic Tunable Filters - Free Space (Brimrose Corporation of America, Baltimore, Md., 2014).
4. C. Zhang, H. Wang, & Y. Qiu, "Study of the Imaging Performance for a Noncollinear Acousto-Optic Tunable Filter", 2010 Symposium on Photonics and Optoelectronics Chengdu, China, 1-4. (2010).
5. N. S. Prasad, "Deep-UV based acousto-optic tunable filter for spectral sensing applications", Int. J. High Speed Electron. Syst. 17, 857-866 (2007).
6. V. B. Voloshinov and N. Gupta, "Ultraviolet-Visible Imaging Acousto-Optic Tunable Filters in KDP", Appl. Opt. 43, 3901 (2004).
7. N. Gupta, "Materials for imaging acousto-optic tunable filters", Proc. of SPIE, vol.9100, 91000C (2014).
8. M. Gottlieb, A. P. Goutzoulis, and N. B. Singh, "Fabrication and characterization of mercurous chloride acoustooptic devices", Appl. Opt. 26, 4681-7 (1987).
9. N. Gupta, "Investigation of a mercurous chloride acousto-optic cell based on longitudinal acoustic mode", Appl. Opt. 48, C151 (2009).
10. A. S. Shcherbakov, Je. Maximov, and S. E. Balderas Mata, "Shaping the dissipative collinear three-wave coupled states in a two-mode medium with a square-law nonlinearity and linear non-optical losses", J. Opt. A 10, 025001, (2008).
11. Korpel. Acousto-Optics, 2nd Ed., N.-Y., (Marcel Dekker, 1997).
12. V.I. Balakshy, V.N. Parygin, L.I. Chirkov. Physical Principles of Acousto-Optics, Radio I Svyaz, Moscow, (1985).
13. M. P. Shaskolskaya, Acoustic Crystals, Moscow, (Nauka, 1982).
14. C. Chang, Handbook of Optics, Volume II, Chapter 12, 2nd. Ed., edited by M. Bass, (McGraw Hill, 1994).
15. F. Nye, Physical Properties of Crystals: Their Representation by Tensors and Matrices, (Oxford University Press, 1985).
16. W. R. Klein and B. D. Cook, "Unified approach to ultrasonic light diffraction", IEEE Trans. Sonics & Ultrasonics, SU-14, 123 - 134 (1967).
17. W. Goodman, Introduction to Fourier optics, 3rd Ed.(Viva Books, 2007).
18. A. S. Shcherbakov, A. O. Arellanes, S. A. Nemov, "Transmission function collinear acousto-optical interaction occurred by acoustic waves of finite amplitude", J. Opt. Soc. Am. B, vol. 30, No. 12, 3174-3183, (2013).
19. V. Ya. Molchanov, V. M. Lyuty, V. F. Esipov, S. P. Anikin, O. Yu. Makarov, and N. P. Solodovnikov, "An Acousto-Optical Imaging Spectrophotometer for Astrophysical Observations", Astronomy Letters, Vol. 28, No. 10, pp. 713-720 (2002).

20. O. Korablev, J-L. Bertaux, A. Grigoriev, E. Dimarellis, Yu. Kalinnikov, A. Rodin, C. Muller, D. Fonteyn, "An AOTF-based spectrometer for the studies of Mars atmosphere for Mars Express mission", *Advances in Space Research*, 29 (2), pp. 143–150 (2002)
21. O. Korablev, A. Fedorova, J.L. Bertaux, A.V. Stepanov, A. Kiselev, Yu.K. Kalinnikov, A.Yu. Titove, F. Montmessin, J.P. Dubois, E. Villard, V. Sarago, D. Belyaev, A. Reberac, E. Neefs, "SPICAV IR acousto-optic spectrometer experiment on Venus Express", *Planetary and Space Science* Vol. 65, Issue 1, pp. 38–57 (2012).